Optics Letters

Ultra-compact InGaAs/GaAs nano-ridge laser monolithically grown on 300 mm silicon substrate

Z. Ouyang,[1,*] E. M. B. Fahmy,[1] D. Colucci,[1,2] A. A. Yimam,[1] J. Van Campenhout,[2] B. Kunert,[2] and D. Van Thourhout[1]

[1] Gent University-imec, Photonics Research Group, INTEC Department, iGent, Technologiepark-Zwijnaarde 126, 9052 Ghent, Belgium
[2] IMEC, Kapeldreef 75, 3001 Heverlee, Belgium
*Zhongtao.Ouyang@Ugent.be

Received 14 January 2025; revised 10 March 2025; accepted 12 March 2025; posted 17 March 2025; published 27 March 2025

Compact and low-threshold III–V semiconductor lasers are considered to be promising light sources for the silicon photonics platform, as they could offer a small footprint and low energy consumption. However, the significant lattice mismatch between III–V materials and silicon poses a fundamental challenge for the monolithic integration of such lasers on a silicon substrate. Using aspect ratio trapping and nano-ridge engineering, it has been shown this challenge can be overcome. However, thus far, only devices with cavity lengths of several hundred micrometers have shown a laser operation. Here, we show what we believe to be a novel approach whereby an amorphous silicon grating is deposited on the sidewalls of the nano-ridge, allowing for much stronger feedback and much shorter cavity lengths. Based on this approach, we achieved lasing with a threshold density of 9.9 kW/cm^2 under pulsed optical pumping, for a device with a cavity length as small as ~16 µm. The side-mode suppression ratio and linewidth of the laser reach 24 dB and 1.25 nm under 25 kW/cm^2. This laser not only demonstrates the high quality of the epitaxial material but also establishes a novel route to realize an ultra-compact electrically driven light source for future high-density and massively scalable silicon photonic integrated circuits. © 2025 Optica Publishing Group. All rights, including for text and data mining (TDM), Artificial Intelligence (AI) training, and similar technologies, are reserved.

https://doi.org/10.1364/OL.555718

Introduction. The exponential growth of data traffic will require efficient chip-to-chip and on-chip optical interconnection methods with low energy consumption and high-density integration [1,2]. The silicon photonics platform has attracted significant attention over the past few decades due to its potential use in such applications. However, the lack of a practical and ultra-compact laser directly integrated on this platform is a major roadblock to the further development of scalable silicon photonic circuits. Given silicon's indirect bandgap and associated low emission efficiency, the integration of III–V lasers has been extensively studied over the last decade using various approaches, but all have their inherent limitations [3–6]. Recently, we have demonstrated a new method to grow high-quality III–V materials directly on silicon substrates without introducing a thick buffer layer. Compared to other methods, our pioneering nano-ridge engineering technique [7,8] offers distinct advantages in terms of device scalability and integration density.

In our previous work, we realized laser cavities by defining an etched grating inside or a metal grating on top of the nano-ridge, resulting in small coupling coefficients and hence long cavities (more than 100 µm) [9–11]. Further footprint reduction and device miniaturization are critical to increase the integration density. Therefore, in this work, high-refractive-index amorphous silicon (aSi) gratings were deposited on the sides of the nano-ridge for enhancing the interaction with the guided mode and facilitating reduction of the cavity length.

Section 2 describes the design of compact nano-ridge lasers with a sidewall grating (SG) and compares them with lasers using a grating on top (TG). This section also presents characterization of the nano-ridges using scanning electron microscopy (SEM) and photoluminescence (PL) spectroscopy and introduces the fabrication process.

In Section 3, we demonstrate characterization results for the fabricated laser devices with both sidewall and top gratings. A single-mode operation is observed, and the effect of varying the grating length is investigated. Also, the effect of the grating width and height is investigated.

Design and fabrication. *Two strategies for compact devices.* For the design of the sidewall grating laser (SGL) cavities and top grating laser (TGL) cavities, we used a 3D finite-difference time-domain (3D-FDTD) solver with Bloch boundary conditions (BC). The simulation models for both types of devices and the definition of the most relevant parameters, the grating width W_{aSi} (for SGL), and grating height H_{aSi} (for TGL) are depicted in Figs. 1(a) and 1(b). Figures 1(c) and 1(d) show the lowest order transverse electric (TE)-like modes for both device models with $W_{aSi} = 200$ nm for the SGL and $H_{aSi} = 200$ nm for the TGL. The nano-ridge itself has a height $H_{NR} = 452$ nm and a width $W_{NR} = 334$ nm. The trench width is 60 nm. The field distribution was calculated, assuming a 50% duty cycle for the gratings, with the cross section taken in the high-index region. Figures 1(c) and 1(d) show that the mode is strongly confined inside the nano-ridge.

Nano-ridge characterization and laser design. These laser structures were grown by metal organic vapor phase epitaxy (MOVPE) on a silicon substrate containing narrow trenches patterned in a SiO_2 layer. Through a combination of aspect

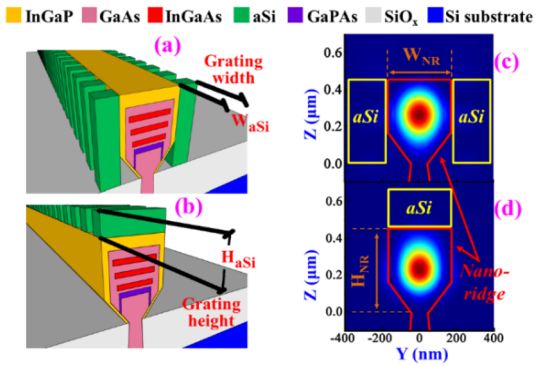

Fig. 1. Device models with the definition of W_{aSi}, and H_{aSi} for the (a) SG and (b) TG. The lowest order transverse electric (TE)-like mode from the models with (c) $W_{aSi} = 200$ nm SG and with (d) $H_{aSi} = 200$ nm TG.

ratio trapping (ART) and nano-ridge engineering (NRE), a nano-ridge with high crystal quality and a large III–V material volume was obtained. The details of the epitaxy process can be found in previous reports [7–11]. The material quality of the nano-ridge was characterized by PL measurements at room temperature. The measurement details were provided in previous reports [9–11]. Figure 2(a) presents the normalized PL spectrum obtained from nano-ridges with different trench sizes under 532 nm continuous-wave pumping with a power density of 4.20 W/cm^2. The PL spectra exhibit a broad peak extending from 960 nm to 1060 nm. Therefore, the cavity design will target this wavelength region. The inset gives a cross-sectional SEM image of a nano-ridge grown from a 60 nm wide trench, after 1 min wet etching using a solution consisting of 50% citric acid, mixed with 30% hydrogen peroxide at a ratio of 10:1. In this image, the InGaP capping layer, the GaAs bulk layer, the InGaAs quantum wells (QWs), the GaPAs carrier blocking layer, and the GaAs trench are clearly visible. From this SEM image, we find the height and width of the nano-ridge to be $H_{NR} = 452$ nm and $W_{NR} = 334$ nm, respectively. These dimensions are used as the starting point for the simulations discussed below.

The interaction between the guided mode and the gratings was investigated by simulating the quality factor (Q-factor) and the confinement of the optical mode in the grating and the quantum wells, using a 3D-FDTD solver with perfectly matched layer and Bloch boundary conditions. All simulations were carried out for a wavelength of 1016 nm, the peak of the PL spectrum for the 60 nm nano-ridge. To simplify the fabrication process, the duty cycle of both the SG and TG was kept at 50%. The period of the grating was optimized to match the PL peak. Figure 2(b) presents the calculated Q-factor for different structures, as a function of the number of periods. S1, S2, and S3 are the SGL devices for which the width of the nano-ridge was varied (W_{NR} is 200 nm, 267 nm, and 334 nm for S1, S2, and S3, respectively). The height of the nano-ridge and the thickness of the grating are kept constant at $H_{NR} = 452$ nm and $W_{aSi} = 200$ nm. S4 is a TGL device with $H_{NR} = 452$ nm, $W_{NR} = 334$ nm, and $H_{aSi} = 200$ nm. The latter is chosen to allow for a direct comparison with the SGL device. All dimensions of simulated devices are given in Table 1.

It is obvious that for all devices, the Q-factor increases with increasing number of periods. Further, for the SGL devices, the Q-factor increases faster for the narrower nano-ridges. This is

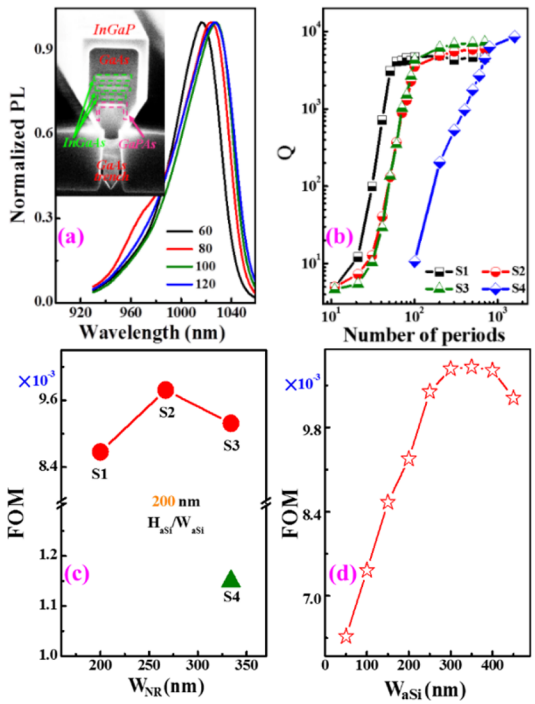

Fig. 2. (a) PL spectra obtained from nano-ridges with 60 nm, 80 nm, 100 nm, and 120 nm trench widths under 532 nm continuous-wave pumping with a power density of 4.20 W/cm^2. Inset: cross-sectional SEM image of the nano-ridge with H_{NR} and W_{NR} of 452 nm and 334 nm (60 nm trench width). (b) Simulated Q-factor for devices S1–S4 as defined in the text, for varying number of periods. (c) Relationship between FOM and W_{NR} for the same devices S1–S4. (d) FOM as function of W_{aSi} for SGL with $W_{NR} = 334$ nm.

a result of the increasing overlap of the optical mode with the grating. On the other hand, the Q-factor saturates at a slightly higher value for the wider devices and for the top grating. Finally, for the shorter gratings, the SGL devices always exhibit a higher Q-factor than the TGL devices.

These simulations show that, in particular for the SGL devices, a narrower nano-ridge results in a stronger interaction of the mode with the grating and hence potentially shorter devices. However, reducing the nano-ridge width also results in a reduced confinement in the QWs and hence a reduced modal gain. To further explore this trade-off, we defined the figure of merit (FOM) = $\Gamma_{aSi}\Gamma_{QW}$, with Γ_{aSi} as the ratio of the integrated electric field intensity in the aSi grating to the one in the whole simulation region and Γ_{QW} as similarly defined for the QWs. Figure 2(c) shows this FOM for the 4 devices previously introduced. For all SGL devices, the FOM is significantly larger than that for the TGL. In addition, the FOM for the SGL devices shows an optimum for W_{NR}~260 nm. The dependence of the FOM on the nano-ridge width is limited, however, and all experimental results were obtained for devices with $W_{NR} = 334$ nm as these were readily available. Figure 2(d) shows how the FOM varies for a SGL device, as a function of W_{aSi} (with $W_{NR} = 334$ nm). Increasing W_{aSi} increases the confinement in the grating and leads to an increased FOM. After reaching a maximum, the FOM decreases again as the mode shifts to the grating region and the overlap with the QWs decreases. Experimentally, we found aSi grating teeth wider than 200 nm bended and touched

each other after processing due to the high aspect ratio and the weak adhesion between the III–V material and the aSi grating. Thus, in the remainder of this work, we mostly focus on devices with $W_{aSi} = 200$ nm.

Fabrication process. Following the design, the SGL devices were fabricated using the process outlined in Fig. 3(a). First, part of the nano-ridges in the dense array were removed to reduce the overall filling ratio of the nano-ridge pattern and allow for complete aSi filling, using a combination of electron-beam lithography (EBL) and plasma etching. We used hydrogen silsesquioxane (HSQ) resist, developed in a 1:3 mixture of AZ400 K and DI water. The non-protected nano-ridges were removed using inductively coupled plasma reactive ion etching (ICP-RIE) with BCl_3/N_2, and the remaining HSQ resist was removed by a buffered oxide etching (BOE) solution. Then, a ~600 nm aSi thin film was deposited using a plasma-enhanced chemical vapor deposition (PECVD). Next, the aSi thin film was uniformly etched using a CHF_3/H_2 gas mixture through ICP-RIE, leaving only the aSi on the sidewalls. To protect the aSi layer from the HSQ developer used in the subsequent lithography step, ~40 nm SiO_x was deposited using PECVD. Then, a second EBL step was used to define the grating in HSQ. Finally, the aSi grating structures on both sides of the nano-ridge and a second-order grating coupler were transferred from the HSQ resist to the aSi layer by ICP-RIE etching of the SiO_x layer and the aSi layer with CHF_3/O_2 and $CHF_3/SF_6/H_2$, respectively. The second-order grating is added to allow vertical coupling of the light emission. The process flow of the TGL devices is similar, but does not require the nano-ridge removal and the top aSi etching (see Fig. 3(b)). Also the deposited aSi can be substantially thinner. Figures 3(c) and 3(d) depict a top-view SEM image and a tilted SEM image of DFB lasers with $H_{NR} = 452$ nm and $W_{NR} = 334$ nm. Figure 3(e) shows an enlarged view of the aSi grating. The crack visible in the lower part of the grating is aligned with the transition between the angled section at the bottom and the vertical section at the side of the nano-ridge, pointing to a not perfectly conformal deposition of the aSi layer. Also, as the top aSi layer was not fully removed, a shallow TG remains on top of the device. Both imperfections could be improved in the future but at this moment do not seem to influence the operation of the device.

Results and discussion. The devices were characterized under pulsed optical pumping, with a wavelength of 532 nm, a pulse repetition rate of 938 Hz, and a pulse length of 7 ns. The details of the setup were discussed in previous reports [9–11]. Except where otherwise mentioned, the dimensions of the nano-ridges used were those shown in Fig. 2(a) ($H_{NR} = 452$ nm, $W_{NR} = 334$ nm). Figure 4(a) shows the PL spectrum for a SGL device with a grating having 100 periods, $W_{aSi} = 200$ nm, and period $\Lambda = 165$ nm. The total length of the cavity was around 16 µm. The pump power density was 25 kW/cm^2. The peak from the DFB laser is located at 1027 nm, achieving a side-mode suppression ratio of over 24 dB. The linewidth of this laser, obtained from a Gaussian function fitting as shown in the inset, is 1.25 nm and likely limited by the pulsed operating regime. Figure 4(b) shows the light in (pumping power density)–light out (integrated PL) curve for the same device on a logarithmic and a linear (inset) scale. The characteristic S-shaped curve and a clear change of slope (in the inset) are the signature of lasing turn-on. The curve is fitted to a rate equations based model [12,13] giving a value $\beta \sim 0.8\%$ for the

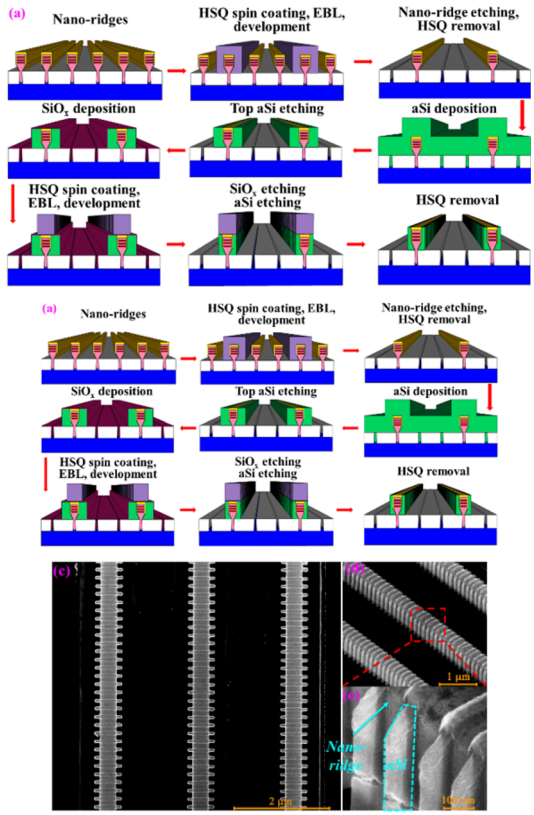

Fig. 3. Process flow diagram illustrating the fabrication steps of a nano-ridge DFB laser with the SG (a) and TG (b). (c) Top-view SEM image of DFB lasers. (d) Tilted SEM image of the same DFB lasers. (e) Enlarged tilted SEM image of the aSi grating on one side.

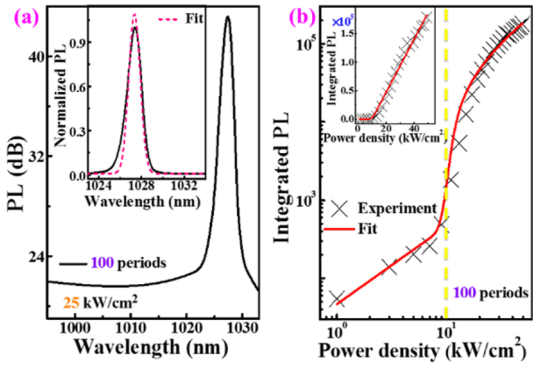

Fig. 4. (a) PL spectrum on a logarithmic scale for a DFB laser with a 100-period SG under 25 kW/cm^2 532 nm pulsed pump power density. Inset: normalized PL spectrum of the same DFB laser, fitted with a Gaussian function. (b) Light in–light out curve on logarithmic and linear (inset) scales of this DFB laser.

coupling efficiency from the spontaneous emission to the cavity mode.

To explore the effect of the grating length on the laser operation, the PL spectra and the light in–light out curves of a series of SGL devices with increasing number of periods were measured. Figure 5(a) shows the PL spectra taken at a pump power density of 25 kW/cm^2. All show a sharp peak, indicating a laser operation. This is further confirmed by the light in–light out curves shown in Fig. 5(b), which all show a clear threshold

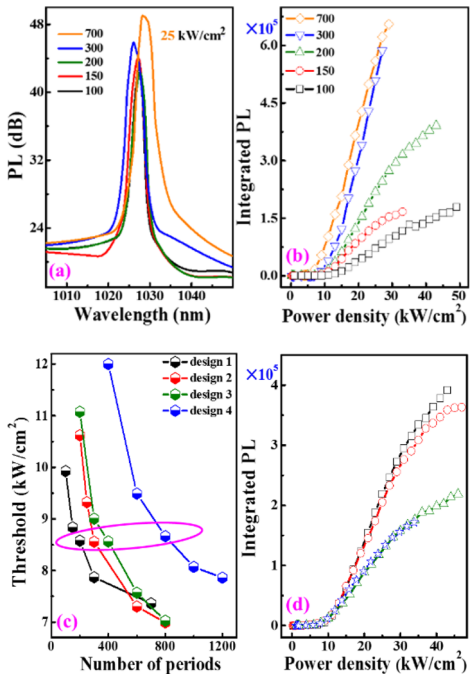

Fig. 5. (a) PL spectrum from SGL devices with various numbers of periods at 25 kW/cm^2. (b) Light in–light out curves on a linear scale of these DFB lasers. (c) Extracted threshold values for devices with designs 1–4 as defined in Table 2, for varying number of periods. (d) Light in–light out curves for the 4 devices within the magenta ellipsis in (c).

Table 1. Dimension of Simulated Devices

	Grating Type	W_{NR} (nm)	H_{NR} (nm)	W_{aSi}/H_{aSi} (nm)
S1	SG	200	452	200
S2	SG	267	452	200
S3	SG	334	452	200
S4	TG	334	452	200

Table 2. Dimension of Fabricated Devices

	Grating Type	W_{aSi}/H_{aSi} (nm)
Design 1	SG	200
Design 2	SG	50
Design 3	TG	100
Design 4	TG	50

behavior. The extracted pump threshold values are shown with black markers (design 1) in Fig. 5(c). As expected, the threshold decreases with increasing grating length.

To investigate the effect of the grating strength, we measured the length dependent light in–light out curves for 4 different device designs, as shown in Table 2. The height of the top grating H_{aSi} is set to 100 nm and 50 nm, to allow comparison with W_{aSi}. The extracted laser thresholds for all 20 devices are shown in Fig. 5(c). Comparing design 1 (black) and design 2 (red), we see that decreasing the thickness of the SG results in a higher threshold for shorter devices, associated with the lower confinement in the grating. For longer devices, the situation reverses, probably due to lower scattering losses in the shallow grating devices. This behavior is also expected from the simulations for the Q-factor shown in Fig. 2(b), where we see a higher maximum Q-factor for devices with a weaker grating interaction. Designs 3 and 4, with a TG, require a further increased cavity length to ensure low-threshold lasing. Figure 5(d) shows the light in–light out curves for the 4 devices within the magenta ellipsis, which all exhibit a similar lasing threshold pump density. Here, the effect of increasing the grating strength is even more obvious, with design 4 requiring 4 times the number of periods for reaching the same threshold density as design 1. Note that this effect would be even more pronounced if we referred to the absolute pump power (i.e., the pump power density multiplied by the device surface).

Conclusion. We proposed a novel approach for realizing compact laser cavities, monolithically integrated on a silicon substrate, using an amorphous silicon grating deposited at the sides of a nano-ridge. By modifying the nano-ridge width or the grating thickness, the interaction of the lasing mode with the grating can be controlled and a high Q-factor can be obtained, even for cavities shorter than 20 µm. Compared to approaches based on etched gratings or photonic crystals, the deposited grating does not deteriorate the material quality [14]. Under pulsed optical pumping, ~9.9 kW/cm^2 lasing threshold was observed for a DFB laser with a cavity length of only ~16 µm (100 periods). The spectrum reveals a single-mode operation with more than 24 dB side-mode suppression ratio. This result once again demonstrates the high quality of the epitaxial material obtained using the nano-ridge approach. Recently, also lasing under electrical injection has been demonstrated for nano-ridge based devices [15]. However, the weak feedback in these devices resulted in a cavity length of 1–2 mm. The high contrast gratings demonstrated in the current work open up the road toward realizing much more compact electrically injected devices that can be used in high-density optical interconnects and other high volume applications based on silicon photonics.

Funding. HORIZON EUROPE European Research Council (884963 (ERC AdG NARIOS)); Interuniversitair Micro-Electronica Centrum VZW Industry-Affiliation Optical I/O R&D programme); China Scholarship Council.

Disclosures. The authors declare no conflicts of interest.

Data availability. Data underlying the results presented in this paper are not publicly available at this time but may be obtained from the authors upon reasonable request.

REFERENCES

1. D. A. Miller, Proc. IEEE **97**, 1166 (2009).
2. A. Shacham, K. Bergman, and L. P. Carloni, IEEE Trans. Comput. **57**, 1246 (2008).
3. H. Liu, J. Lee, Y. Zhao, *et al.*, Opt. Express **24**, 16258 (2016).
4. M. R. Billah, M. Blaicher, T. Hoose, *et al.*, Optica **5**, 876 (2018).
5. J. Zhang, G. Muliuk, J. Juvert, *et al.*, APL Photonics **4**, 1-10 (2019).
6. J. Yang, P. Jurczak, F. Cui, *et al.*, J. Cryst. Growth **514**, 109 (2019).
7. M. Baryshnikova, Y. Mols, Y. Ishii, *et al.*, Crystals **10**, 330 (2020).
8. D. Van Thourhout, Y. Shi, M. Baryshnikova, *et al.*, Future Directions in Silicon Photonics **101**, 283 (2019).
9. Y. Shi, Z. Wang, J. Van Campenhout, *et al.*, Optica **4**, 1468 (2017).
10. Y. Shi, M. Pantouvaki, J. Van Campenhout, *et al.*, Opt. Express **29**, 14649 (2021).
11. D. Colucci, M. Baryshnikova, Y. Shi, *et al.*, Opt. Express **30**, 13510 (2022).
12. H. Yokoyama and S. D. Brorson, J. Appl. Phys. **66**, 4801 (1989).
13. K. A. Shore and M. Ogura, Opt. Quantum Electron. **24**, S209 (1992).
14. Z. Ouyang, D. Colucci, E. M. B. Fahmy, *et al.*, Opt. Lett. **49**, 4741 (2024).
15. Y. De Koninck, C. Caer, D. Yudistira, *et al.*, Nature **637**, 63 (2025).